arXiv:1405.3291v1 [astro-ph.EP] 13 May 2014

Gravito-Turbulent Disks in 3D: Turbulent Velocities vs. Depth

Ji-Ming Shi[1,2] and Eugene Chiang[1,2,3]
jmshi@berkeley.edu

ABSTRACT

Characterizing turbulence in protoplanetary disks is crucial for understanding how they accrete and spawn planets. Recent measurements of spectral line broadening promise to diagnose turbulence, with different lines probing different depths. We use 3D local hydrodynamic simulations of cooling, self-gravitating disks to resolve how motions driven by "gravito-turbulence" vary with height. We find that gravito-turbulence is practically as vigorous at altitude as at depth. Even though gas at altitude is much too rarefied to be itself self-gravitating, it is strongly forced by self-gravitating overdensities at the midplane. The long-range nature of gravity means that turbulent velocities are nearly uniform vertically, increasing by just a factor of 2 from midplane to surface, even as the density ranges over nearly three orders of magnitude. The insensitivity of gravito-turbulence to height contrasts with the behavior of disks afflicted by the magnetorotational instability (MRI); in the latter case, non-circular velocities increase by at least a factor of 15 from midplane to surface, with various non-ideal effects only magnifying this factor. The distinct vertical profiles of gravito-turbulence vs. MRI turbulence may be used in conjunction with measurements of non-thermal linewidths at various depths to identify the source of transport in protoplanetary disks.

Subject headings: accretion, accretion disks — hydrodynamics — turbulence — protoplanetary disks — methods: numerical — line: profiles

1. INTRODUCTION

How protoplanetary disks transport angular momentum and mass has been a longstanding mystery (e.g., Hartmann et al. 2006). Turbulence driven by the magnetorotational instability (MRI; Balbus & Hawley 1991, 1998) is perhaps the most intensively studied mechanism. Recent studies explore a host of non-ideal magnetohydrodynamic effects that strongly affect the character of transport in poorly ionized disks (e.g., Perez-Becker & Chiang 2011a,b; Bai 2011; Wardle & Salmeron 2012; Bai & Stone 2013; Bai 2013; Simon et al. 2013a,b; Kunz & Lesur 2013; Lesur et al. 2014). Disk self-gravity is another option for sufficiently massive disks (e.g., Paczynski 1978; Gammie 2001; Forgan et al. 2012). Torques could be exerted either by globally coherent spiral structure, or by local density waves that are continuously generated and dissipated in a state of "gravito-turbulence". Non-circular motions, turbulent or otherwise, impact planet and planetesimal formation insofar as they regulate grain growth (e.g., Ormel et al. 2007), the degree to which dust settles and concentrates (e.g., Lee et al. 2010a,b), and how planets migrate (e.g., Nelson & Papaloizou 2004; Laughlin et al. 2004; Rein 2012). Pinning down the nature of turbulence in protoplanetary disks is a first-rank problem.

Spectral line broadening offers empirical constraints on non-circular motions. Using Submillimeter Array observations of the CO $(3-2)$ emission line, Hughes et al. (2011) found that the "turbulent" linewidth (i.e., the Doppler "b"-

[1]Department of Astronomy, UC Berkeley, Hearst Field Annex B-20, Berkeley, CA 94720-3411

[2]Center for Integrative Planetary Science, UC Berkeley, Hearst Field Annex B-20, Berkeley, CA 94720-3411

[3]Department of Earth and Planetary Science, UC Berkeley, 307 McCone Hall, Berkeley, CA 94720-4767

parameter[1]) in the high-altitude outskirts of the HD 163296 disk is ∼300 m/s, about 40% of the local sound speed. This non-thermal linewidth appears consistent with MRI turbulence, but other drivers have not been ruled out. Lines from other transitions would enable us to plumb the depths of turbulence vertically and thereby constrain its origin (Simon et al. 2011; Hughes et al. 2014, in preparation). Similarly illuminating would be radial profiles of non-thermal linewidths (Forgan et al. 2012); these are promised by, e.g., the Atacama Large Millimeter Array.

In this paper we numerically simulate gravito-turbulence in a 3D shearing box. Our goal is to measure how the non-circular motions generated by gravito-turbulence vary with disk altitude. By determining what is distinctive about these vertical profiles, we hope to inform observations of non-thermal linewidths like those pioneered by Hughes et al. (2011), and ultimately to characterize turbulence in disks, protoplanetary or otherwise. We utilize a grid-based code (`Athena`) to resolve stratified, self-gravitating, secularly cooling disks, achieving unprecedentedly high resolution and dynamic range in the vertical direction (cf. Forgan et al. 2012). Radiative cooling is treated in the optically thin limit in which every grid cell cools independently of every other. We experiment with two cooling prescriptions: either the cooling time is fixed in space and time ("constant cooling time") or it depends on the local temperature ("optically-thin thermal cooling"). Our disks attain a state of steady gravito-turbulence in which the imposed cooling is balanced by compressive heating driven by gravitational instability.

We describe our numerical methods in §2. Results are presented in §3, and placed into physical context in §4, together with an outlook.

2. METHODS

The equations we solve are listed in §2.1; a description of our code and our adopted boundary conditions are given in §2.2; initial conditions and simulation parameters are provided in §2.3; and some averages used to diagnose our results are defined in §2.4.

[1]Not to be confused with the cooling parameter b introduced later in our paper.

2.1. Equations Solved

We solve the hydrodynamic equations governing three-dimensional, self-gravitating, stratified accretion disks, including the effects of secular cooling. The disk is modeled in the local shearing box approximation. In a Cartesian reference frame corotating with the disk at fixed orbital frequency $\Omega\hat{\mathbf{z}}$, the equations solved by our code are as follows:

$$\frac{\partial \rho}{\partial t} + \nabla \cdot (\rho \mathbf{v}) = 0\,, \quad (1)$$

$$\frac{\partial \rho \mathbf{v}}{\partial t} + \nabla \cdot (\rho \mathbf{v}\mathbf{v} + P\mathbf{I} + \mathbf{T}_{\rm g}) = -2\rho\Omega\hat{\mathbf{z}} \times \mathbf{v} + 2q\rho\Omega^2 x\hat{\mathbf{x}} - \rho\Omega^2 z\hat{\mathbf{z}}\,, \quad (2)$$

$$\frac{\partial E}{\partial t} + \nabla \cdot (E + P)\mathbf{v} = -\rho\mathbf{v} \cdot \nabla\Phi + \rho\Omega^2 \mathbf{v} \cdot (2qx\hat{\mathbf{x}} - z\hat{\mathbf{z}}) - \rho\mathcal{L}\,, \quad (3)$$

$$\nabla^2\Phi = 4\pi G\rho\,, \quad (4)$$

where $\hat{\mathbf{x}}$ points in the radial direction, ρ is the gas mass density, $\mathbf{v}$ is the gas velocity, P is the gas pressure, Φ is the disk's self-gravitational potential, $q = 3/2$ is the Keplerian shear parameter,

$$E = U + K = \frac{P}{\gamma - 1} + \frac{1}{2}\rho v^2 \quad (5)$$

is the sum of the internal energy density U and bulk kinetic energy density K for an ideal gas with specific heat ratio $\gamma = 5/3$, and

$$\mathbf{T}_{\rm g} = \frac{1}{4\pi G}\left[\nabla\Phi\nabla\Phi - \frac{1}{2}(\nabla\Phi)\cdot(\nabla\Phi)\,\mathbf{I}\right] \quad (6)$$

is the gravitational stress tensor with identity tensor $\mathbf{I}$.

We consider two prescriptions for the volumetric cooling rate (a.k.a. volume emissivity) $\rho\mathcal{L}(\rho, U)$. In the first case, we have

$$\rho\mathcal{L} = U/t_{\rm cool} = \Omega U/\beta \quad \text{(constant cooling time)} \quad (7)$$

with $\beta \equiv \Omega t_{\rm cool}$ constant everywhere. The assumption of constant cooling time $t_{\rm cool}$ is adopted by many 2D (e.g., Gammie 2001; Johnson & Gammie 2003; Paardekooper 2012) and 3D (e.g., Rice et al. 2003; Lodato & Rice 2004, 2005; Mejía et al. 2005; Cossins et al. 2009; Meru & Bate 2011) simulations of self-gravitating disks. This prescription enables direct experimental control over the rate of energy loss.

In our second treatment of cooling, we assume that the cooling radiation is thermal and that the disk is optically thin to such radiation. Then every parcel of gas has its own cooling time $t_{\rm cool} = U/(\rho\mathcal{L}) \propto T/\mathcal{L} \propto 1/(T^3\kappa)$, with $\mathcal{L} \propto T^4\kappa$ for temperature T and opacity κ. We assume constant κ, as would be the case if the cooling radiation were emitted by grains in the geometric optics limit (so that κ is independent of T), and if the grains were uniformly mixed with gas (so that κ is independent of ρ). These assumptions may hold in the outermost portions of gravito-turbulent disks, where opacities are dominated by mm–cm sized dust particles and where strong vertical flows in dense gas can keep such particles aloft. Other opacity laws characteristic of molecules or H^- may obtain in the hotter inner regions where dust sublimates (cf. Bell & Lin 1994). For constant κ we have $t_{\rm cool} = b(\rho/P)^3$ for constant b, or equivalently

$$\rho\mathcal{L} = \frac{1}{b(\gamma-1)}\frac{P^4}{\rho^3} \quad \text{(optically thin, thermal cooling)}. \tag{8}$$

In our experiments, we choose b such that the cooling time averaged over our simulation domain equals some desired value.

2.2. Code Description and Boundary Conditions

Our simulations are run with `Athena` (Stone & Gardiner 2010). We adopt the van Leer integrator (van Leer 2006; Stone & Gardiner 2009), a piecewise linear spatial reconstruction in the primitive variables, and the HLLC (Harten-Lax-van Leer-Contact) Riemann solver. We solve Poisson's equation using fast Fourier transforms (Koyama & Ostriker 2009; Kim et al. 2011). Self-gravity is added to the momentum equation in a conservative form (as shown in equation 2), but added to the energy equation (3) as a source term; thus the total energy does not conserve to round-off error (for a more accurate algorithm, see Jiang et al. 2013). We have verified, however, that the error introduced in our treatment of energy is negligible, as we reproduce well the analytic result of Gammie (2001) for how the stress varies with cooling—this dependence essentially reflects energy conservation (see our §3.1.2 and Figure 4).

Boundary conditions for our hydrodynamic flow variables (ρ, $\mathbf{v}$, U, but not the self-gravitational potential Φ) are shearing-periodic in radius (x), periodic in azimuth (y), and outflow in height (z). The Poisson solver for Φ implements shearing-periodic boundary conditions in x, periodic boundary conditions in y, and vacuum boundary conditions in z (Koyama & Ostriker 2009; Kim et al. 2011). The ghost-cell values for Φ in z are set by solving the finite-difference form of the Poisson equation. Note that the version of `Athena`'s shearing-box Poisson solver that we downloaded produces velocities in the simulation domain that are discontinuous with those in ghost cells if the box is too large in the x-direction and if the Courant number (governing our timestep) $\gtrsim 0.4$–0.5. We found that we could eliminate these discontinuities by reducing the Courant number to $\sim$0.1, but did not implement a deeper fix.

We use orbital advection algorithms to shorten the timestep and improve conservation (Masset 2000; Johnson et al. 2008; Stone & Gardiner 2010). Upon adding cooling as an explicit source term in equation (3), we also modify the timestep Δt to equal $\min(\Delta t_0, \epsilon\, t_{\rm cool})$, where Δt_0 is `Athena`'s usual Courant-limited timestep, $t_{\rm cool}$ is evaluated for every cell, and $\epsilon = 0.02$, small enough to resolve the cooling history. Typically Δt_0 is 10^2–10^4 times shorter than $\min(t_{\rm cool})$.

2.3. Initial Conditions, Run Parameters, and Box Sizes

For our constant cooling simulations, we take $\beta \equiv \Omega t_{\rm cool} \in \{3, 4, 5, 8, 10, 20, 40, 80\}$. Initial conditions for $\beta \in \{20, 40, 80\}$ are derived from $\beta = 10$ by "morphing": we initialize $\beta = 20$ with the final gravito-turbulent outcome from $\beta = 10$; $\beta = 40$ is initialized with the final outcome from $\beta = 20$; and $\beta = 80$ is initialized with the final outcome from $\beta = 40$. Initial conditions for $\beta < 10$ are derived directly from the final outcome of $\beta = 10$. Morphing has the advantage that for each β, the disk can adjust more quickly to its quasi-equilibrium state, i.e., we bypass as much as possible initial violent transients. In any case, we take care to run every simulation for long enough duration (typically several cooling times) that a steady gravito-turbulent state is reached in which time-averaged quantities such as rms density and velocity fluctuations have converged to unique values. All simulations with optically thin cooling are initialized with the outcome from $\beta = 10$. See Ta-

ble 1 for run parameters.

For $\beta = 10$, the initial vertical density profile is derived semi-analytically. We solve for vertical hydrostatic equilibrium including self-gravity (cf. Shi & Chiang 2013):

$$\frac{1}{\rho}\frac{dP}{dz} = -\Omega^2 z - 4\pi G \int_0^z \rho(z')dz' \qquad (9)$$

for a polytropic gas $P = K\rho^\gamma$ (the polytropic assumption is used only for this initialization; the subsequent evolution obeys the full energy equation as described in §2.1). A non-dimensional, differential form of (9) reads:

$$\frac{d^2\tilde{\rho}}{d\tilde{z}^2} + \frac{\gamma-2}{\tilde{\rho}}\left(\frac{d\tilde{\rho}}{d\tilde{z}}\right)^2 + Q_0^2\tilde{\rho}^{2-\gamma} + \frac{2}{h}\tilde{\rho}^{3-\gamma} = 0 \quad (10)$$

where $\tilde{\rho} \equiv \rho/\rho_0$, $\rho_0 \equiv \rho(z=0)$, $\tilde{z} \equiv z/H_{\rm sg}$, $H_{\rm sg} \equiv [c_{\rm s}(0)]^2/(\pi G\Sigma_0)$ is a fiducial lengthscale for a self-gravitating disk, $c_{\rm s}(0) = \sqrt{\gamma P(z=0)/\rho_0} = \sqrt{K\gamma\rho_0^{\gamma-1}}$ is the initial sound speed at the midplane, $\Sigma_0 \equiv 2\rho_0 H$ is the surface density for an effective half-thickness H, $h \equiv H/H_{\rm sg}$, and Toomre's initial $Q_0 \equiv c_{\rm s}(0)\Omega/(\pi G\Sigma_0)$. From these definitions,

$$h = \frac{1}{2}\int_{-\infty}^{\infty} \tilde{\rho}\, d\tilde{z}\,. \qquad (11)$$

Upon setting $Q_0 = 1$ and $\gamma = 5/3$, we iteratively solve equations (10) and (11) for $\tilde{\rho}(\tilde{z})$ and h (starting with an initial guess for h). We find that $h = 0.4703$, and show the density profile in Figure 1. From these parameters, plus our code units ($\rho_0 = H = \Omega = 1$), it follows that $c_{\rm s}(0) = 2.126$ (equivalently $K = 2.712$) and $G = 0.3384$.

We verified by direct simulation that these initial conditions yield disks that are stable to perturbations in the absence of cooling ($\beta = \infty$). In our experiments with $\beta = 10$, we initialize the disk with random, cell-to-cell velocity perturbations up to $0.1c_{\rm s}(0)$ for $|z| < 2H$. These random velocities are introduced only at $t = 0$; they are not driven. Our experiments with other β's (initialized according to our "morphing" procedure) and optically-thin cooling (initialized with the end state of our $\beta = 10$ run) begin turbulent, and so for these simulations we introduce no further perturbation.

Our boxes span $[-32H, 32H]$ in the x and y directions, and $[-6H, 6H]$ in z. Our standard resolution is $256\times256\times48$ (4 cells per H). We also experiment with a higher resolution of $512\times512\times96$ (8 cells per H), and different size boxes (see Table 1).

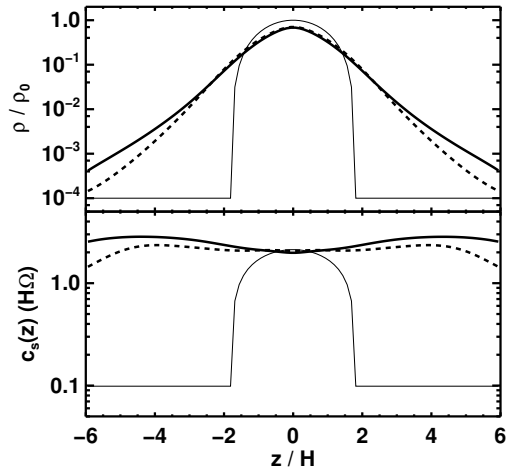

Fig. 1.— *Top*: Density as a function of height, drawn from our static initial conditions (thin solid line); from the fully gravito-turbulent state to which our $\beta = \Omega t_{\rm cool} = 10$ simulation (tc=10.hi) relaxes, time-averaged from $t = 200$–$300\Omega^{-1}$ (thick solid line); and from the gravito-turbulent outcome of our optically-thin thermal cooling simulation b=500.hi, similarly time-averaged (dashed line). *Bottom:* Same as top but for sound speed. In both our cooling prescriptions, our disks are optically thin in the sense that every grid cell cools independently of every other grid cell; we find that such disks, when heated by gravito-turbulence, are nearly isothermal.

We found in our simulations that the code timestep was often limited by the dynamics of low-density gas at the vertical boundaries of our box, where pressure gradients were especially large. To avoid catastrophic reductions in the timestep, we set a floor on the density of $10^{-4}\rho_0$. Lowering this floor by an order of magnitude reduced the timestep by at least 30% but did not significantly alter our results.

2.4. Diagnostic Averages

To facilitate analysis and obtain statistical properties of our 3D time-dependent flows, we define a few ways to average physical variables. The first is a volume (box) average:

$$\langle X \rangle \equiv \frac{\int X\, dxdydz}{\int dxdydz}\,. \qquad (12)$$

We can also weight by density:

$$\langle X \rangle_\rho \equiv \frac{\int \rho X \, dxdydz}{\int \rho \, dxdydz} \,. \tag{13}$$

To see the height dependence of variables, we define a horizontal average using

$$\langle X(z) \rangle \equiv \frac{\int X \, dxdy}{\int dxdy} \,. \tag{14}$$

Time averaging is denoted

$$\langle X \rangle_t \equiv \frac{\int X \, dt}{\int dt} \,. \tag{15}$$

Sometimes we will combine averages: e.g., $\langle \langle X \rangle \rangle_t$.

3. RESULTS

Results from our constant cooling time and optically-thin thermal cooling experiments are given in §3.1 and §3.2, respectively. Some time-and-space-averaged properties of our simulations are listed in Table 1.

3.1. Constant Cooling Time (Constant $\beta \equiv \Omega t_{\rm cool}$)

We begin by presenting our standard $\beta = 10$ run in §3.1.1. How the stress scales with cooling rate and height is discussed in §3.1.2, and how turbulent (read: non-circular) velocities depend on disk altitude is described in §3.1.3.

3.1.1. Standard Run ($\beta = 10$)

The simulations with $t_{\rm cool} = 10\Omega^{-1}$ (dubbed tc=10 at standard resolution and tc=10.hi at high resolution in Table 1) start from the hydrostatic equilibrium solution described in section 2.3 and evolve for $30t_{\rm cool} = 300\Omega^{-1}$. The evolution of the disk as a whole can be followed by constructing an effective Toomre's Q:

$$Q \equiv \frac{\langle c_{\rm s} \rangle_\rho \Omega}{\pi G \langle \Sigma \rangle} \tag{16}$$

where $\langle \Sigma \rangle$ is the vertical surface density averaged horizontally and $\langle c_{\rm s} \rangle_\rho \equiv \langle \sqrt{\gamma P/\rho} \rangle_\rho$ is the density-weighted, box-averaged sound speed.

Figure 2 displays the time evolution of Q. The disk settles into steady gravito-turbulence after an initial transient phase lasting $\sim 50\Omega^{-1}$. The transient phase is violent: the cooling disk collapses under its own weight during the first $10\Omega^{-1}$; rebounds vertically as gas becomes strongly heated by shocks from $t = 10\Omega^{-1}$ to $25\Omega^{-1}$; and relaxes from $t = 25\Omega^{-1}$ to $50\Omega^{-1}$ into a quasi-steady state that lasts the remainder of the simulation. During the rebound phase, about 10% of the total mass in the box is lost through the vertical boundaries. This initial mass loss should be of no consequence as we are interested in the final dynamical equilibrium attained by the disk, i.e., the steady self-regulated state in which heating driven by gravitational instability closely balances the imposed cooling.

The final equilibrium density profile is broader than our initial profile, as illustrated in Figure 1. In the final state, mass continues to be lost through the top and bottom of the box, but at a rate so slow ($\lesssim$ 10% from $t = 50$–$300\Omega^{-1}$) that we discern no obvious long-term trend in any other statistical property that we measure. This is demonstrated in Figure 2, which attests that in self-regulated gravito-turbulence (for $\beta = 10$), Q hovers around 1.33; density fluctuations

$$\delta\rho = \rho(x, y, z) - \langle \rho(z) \rangle \tag{17}$$

are on the order of unity when normalized to the average local density; velocity fluctuations

$$\delta v = \sqrt{v_x^2 + \delta v_y^2 + v_z^2} \tag{18}$$

are mildly sonic (here $\delta v_y = v_y + 3\Omega x/2$ is the non-Keplerian azimuthal velocity); and the Shakura-Sunyaev stress-to-pressure parameter

$$\alpha \equiv \frac{\langle w_{xy} \rangle_\rho}{\langle P \rangle_\rho} \equiv \frac{\langle g_x g_y / 4\pi G + \rho v_x \delta v_y \rangle_\rho}{\langle P \rangle_\rho} \tag{19}$$

fluctuates about 0.055, with the gravitational stress ($g_x g_y / 4\pi G$) exceeding the Reynolds stress ($\rho v_x \delta v_y$) by roughly a factor of 3 (here $g_x \hat{\mathbf{x}} + g_y \hat{\mathbf{y}} + g_z \hat{\mathbf{z}}$ is the local gravitational acceleration). Our definition for α weights by density; it tries to "follow the mass" in our stratified simulations and should be more accurate, e.g., when applied to 2D studies that evolve Σ instead of ρ. In the literature—which reports on simulations that are commonly unstratified—the stress-to-pressure ratio is more often calculated as a volume average

TABLE 1
3D SIMULATIONS OF GRAVITO-TURBULENT DISKS

Name[a]	$\Delta T^{(b)}$ (Ω^{-1})	$\Delta T_{\rm avg}{}^{(c)}$ (Ω^{-1})	$\langle\langle t_{\rm cool}\rangle\rangle_t$ (Ω^{-1})	$\langle\alpha_{\rm Reynolds}\rangle_t{}^{(d)}$ ($\times 10^{-2}$)	$\langle\alpha_{\rm gravity}\rangle_t{}^{(d)}$ ($\times 10^{-2}$)	$\langle\alpha\rangle_t{}^{(d)}$ ($\times 10^{-2}$)	$\langle\alpha'\rangle_t{}^{(d)}$ ($\times 10^{-2}$)	$\langle\langle\delta v^2\rangle_\rho^{1/2}\rangle_t$ ($H\Omega$)	$\langle\langle c_{\rm s}\rangle_\rho\rangle_t$ ($H\Omega$)
tc=3.hi [e]	20	–	3	–	–	–	–	–	–
tc=4.hi	200	100	4	5.69	6.50	12.2	10.0	2.31	1.96
tc=5.hi	200	100	5	4.19	5.82	10.0	8.19	2.20	2.01
tc=8.hi	200	100	8	2.06	4.41	6.47	5.10	1.90	2.07
tc=10	300	100	10	1.88	3.87	5.76	4.24	1.79	2.18
tc=10.dfl	300	100	10	1.35	3.99	5.33	4.14	1.71	2.05
tc=10.lxy128	300	100	10	1.20	4.03	5.23	3.89	1.98	2.12
tc=10.hi	300	100	10	1.70	3.82	5.52	4.06	1.79	2.17
tc=10.hi.dfl	300	100	10	1.72	3.95	5.67	4.19	1.74	2.04
tc=10.hi.lz10	100	50	10	1.98	3.78	5.77	4.09	1.73	2.02
tc=10.hi.lz14	100	50	10	1.22	4.03	5.25	4.09	1.74	2.05
tc=20	150	100	20	0.29	2.55	2.85	2.14	1.35	2.17
tc=20.hi	140	100	20	0.46	2.42	2.88	2.02	1.26	2.07
tc=20.hi.dfl	140	100	20	0.73	2.47	3.20	2.18	1.31	2.11
tc=40	300	200	40	−0.06	1.51	1.44	1.06	0.97	2.10
tc=40.hi	400	200	40	0.27	1.36	1.62	1.03	1.05	2.14
tc=80	400	200	80	0.13	0.76	0.89	0.55	0.85	2.26
tc=80.hi	500	200	80	0.35	0.58	0.93	0.52	1.16	2.26
tc=120.hi	500	200	80	0.14	0.39	0.53	0.31	1.09	2.12
b=100.hi [e]	10	–	< 3	–	–	–	–	–	–
b=500.hi	140	100	9.64	1.67	3.99	5.66	4.02	1.61	2.09
b=500.hi.dfl	140	100	10.6	1.53	3.64	5.17	3.64	1.55	2.07
b=800.hi	240	150	17.1	0.92	2.56	3.47	2.28	1.31	2.15
b=1000.hi	240	150	19.4	0.84	2.29	3.13	2.02	1.28	2.21
b=2000.hi	240	150	28.2	1.02	1.66	2.68	1.50	1.24	2.38
b=3000.hi	240	150	45.8	0.65	1.00	1.66	0.88	1.05	2.40

[a] Our naming convention is as follows: 'tc=n' denotes a constant cooling time simulation with $\beta = \Omega t_{\rm cool} =$ n; 'b=n' denotes a simulation with optically-thin thermal cooling with $b =$ n (see §2.1); '.hi' implies a higher resolution of $512 \times 512 \times 96$ grid cells instead of our standard $256 \times 256 \times 48$; '.dfl' simulations use a density floor equal to $10^{-5}\times$ our initial midplane density (densities that fall below the floor value are set equal to the floor value), whereas our standard simulations use a floor value of $10^{-4}\times$ the initial midplane density; '.lxy128' denotes a wider (but not taller) box that spans $[-64H, 64H]$ in the x and y directions instead of our standard $[-32H, 32H]$; and '.lz10' and '.lz14' denote box heights of $10H$ and $14H$, respectively, instead of our default height of $12H$.

[b] Duration of the simulation.

[c] Time span used for averaging various quantities, measured backward from the end of the run; e.g., a simulation of duration $\Delta T = 200\Omega^{-1}$ for which $\Delta T_{\rm avg} = 100\Omega^{-1}$ takes its averaging interval between times $t_1 = 100\Omega^{-1}$ and $t_2 = 200\Omega^{-1}$.

[d] As defined by equations (19) and (20), respectively, α is the density-weighted average over the simulation domain, and α' is the conventional box averaged value with no density weighting. The total stress $\alpha = \alpha_{\rm Reynolds} + \alpha_{\rm gravity}$.

[e] For these runs, cooling is so rapid that the disk fragments gravitationally.

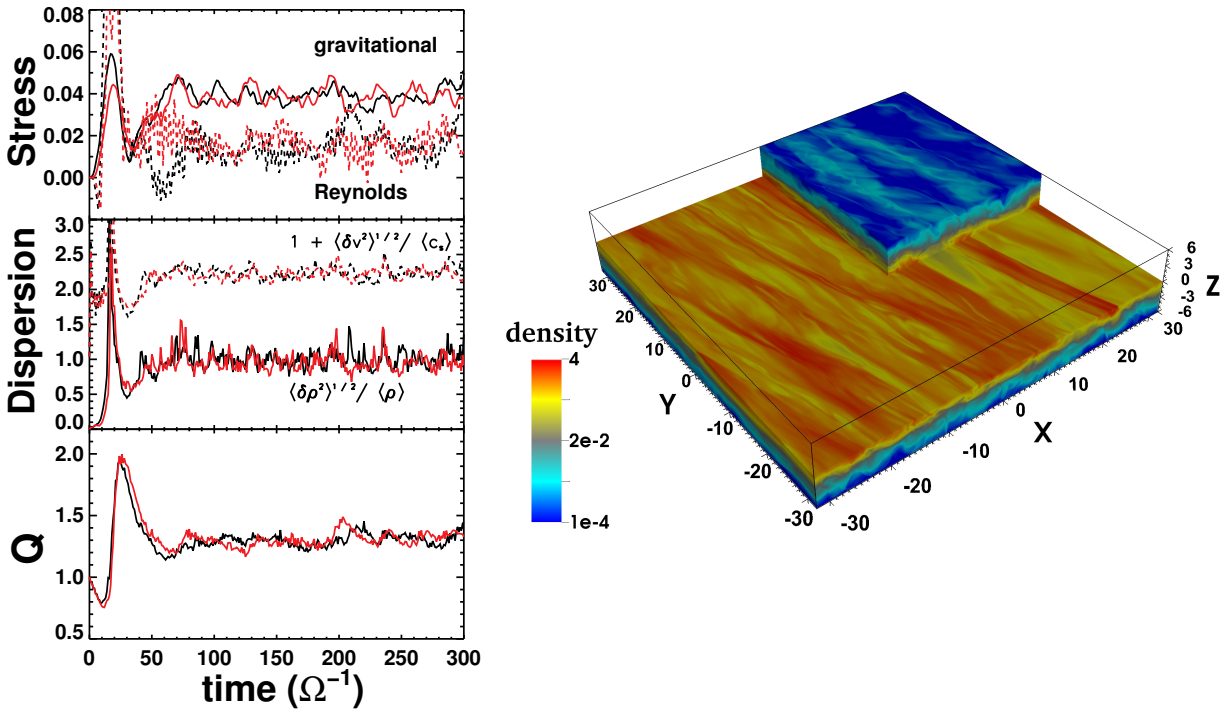

Fig. 2.— Simulation results for constant $t_{\rm cool} = 10\Omega^{-1}$. *Left*: Time histories of the Reynolds and gravitational stresses, normalized as in equation (19) and smoothed by $12\Omega^{-1}$ for clarity; volume-averaged rms density and velocity fluctuations (the latter is offset by 1 for clarity); and Toomre's Q. See text for definitions. Black curves are drawn from our standard resolution simulation (tc=10) and red curves are from our high resolution simulation (tc=10.hi). *Right*: Cutaway view of density on a logarithmic scale at $t = 250\Omega^{-1}$ from our high-resolution simulation.

without weighting by density (e.g., equation 19 in Gammie 2001):

$$\alpha' \equiv \left|\frac{d\ln\Omega}{d\ln R}\right|^{-1}\frac{\int w_{xy}dxdydz}{\int \rho c_{\rm s}^2 dxdydz} = \frac{2}{3\gamma}\frac{\langle w_{xy}\rangle}{\langle P\rangle} \quad (20)$$

where R is disk radius. This conventional α' is 0.5–0.8 times our α in constant cooling time simulations. We calculate both measures of stress in this paper; see, e.g., Table 1. Our results appear robust insofar as doubling the resolution in every direction changes α by just a few percent (compare red and black curves in Figure 2, and see also Table 1).

3.1.2. Stress vs. Cooling Rate and Height: $\alpha(t_{\rm cool}, z)$

All simulations were run for long enough that we can recover steady curves at late times like those shown in Figure 2, enabling us to evaluate meaningful time averages. In only one constant cooling run, tc=3.hi ($\beta = 3$), did the disk fragment instead of settling into steady gravito-turbulence (see also our analogous optically-thin run b=100.hi for which $\beta < 3$, which also fragmented). Thus we establish (for $\gamma = 5/3$) that the collapse criterion in 3D local disks is $t_{\rm cool} \lesssim 3\Omega^{-1}$. This is consistent with the fragmentation boundary reported previously in 2D local (e.g., Gammie 2001) and 3D global studies (e.g., Clarke et al. 2007; but see Meru & Bate 2011, Meru & Bate 2012, and Rice et al. 2014 for cautionary remarks. Figures 3 and 4 show how the density-weighted $\langle\alpha\rangle_t$ and the volume-averaged $\langle\alpha'\rangle_t$—and their gravitational and hydrodynamic components—vary with $t_{\rm cool}$ for our high-resolution runs (time averages are taken over intervals lasting at least

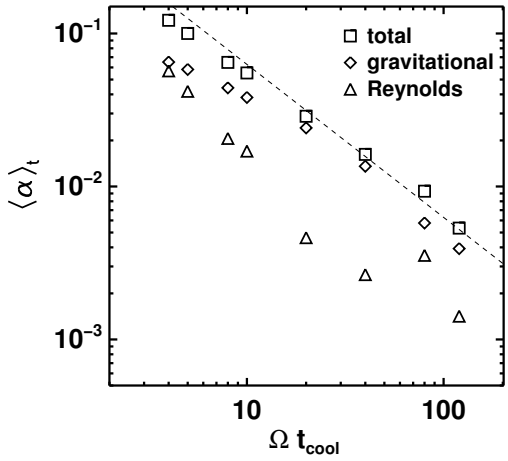

Fig. 3.— Density-weighted time-and-space-averaged stresses α (as defined in equation 19) vs. cooling time for our high-resolution constant β simulations. The dashed line scales as $1/(\Omega t_{\rm cool})$ and is shown for reference. See also Figure 4 which plots the volume-averaged α' without weighting by density.

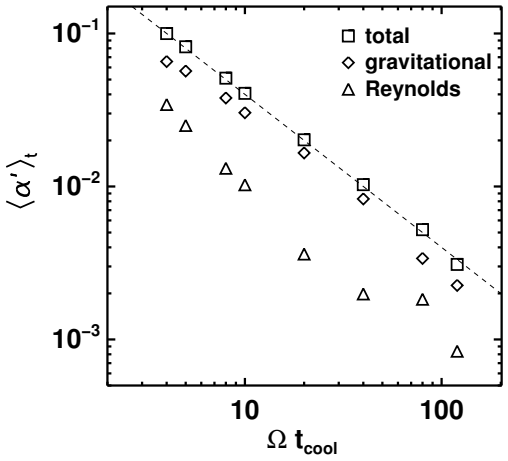

Fig. 4.— The conventional time-and-volume-averaged stresses α' (see equation 20, which is equivalent to equation 19 of Gammie 2001) vs. cooling time for our high-resolution constant β simulations. The dashed line shows the analytic prediction of equation (21) (see also equation 20 of Gammie 2001 for the case of a 2D disk), evaluated for our chosen $\gamma = 5/3$. The simulation results match the analytic formula, implying that our code conserves total energy well.

$100\Omega^{-1}$; see Table 1). Gravitational stresses are observed to exceed hydrodynamic streses by factors of ∼2–5. We find that α and especially α' scale closely with $1/(\Omega t_{\rm cool})$, as expected from energy conservation (Gammie 2001). Figure 4 for α' reveals that our simulation results match the analytic expectation

$$\alpha' = \frac{4}{9\gamma(\gamma-1)}\frac{1}{\Omega t_{\rm cool}} \qquad (21)$$

nearly perfectly for our chosen $\gamma = 5/3$, indicating excellent energy conservation in our code.

A similar scaling of stress with $t_{\rm cool}$ applies at all heights, as demonstrated in Figure 5. Note how the local stress—which is dominated by gravitational forces—diminishes by factors of ∼6–16 from $|z| = H$ to $|z| = 4H$, or roughly as $|z|^{-n}$ with $n = 1.2$–2, by contrast to the density ρ which drops exponentially with height (Figure 1). The comparatively slow drop-off of stress with height arises because gravity is a long-range force: the stress at altitude arises from gravitational forces exerted by density fluctuations near the midplane. We illustrate this in Figure 6 by plotting the contribution to the total gravitational stress exerted at $z = 4H$ from all heights. About 80% of the stress at $z = 4H$ comes from the gravity of the disk between $-H < z < H$.

Total α-values generally change by 10% or less when the resolution is doubled in all directions; when the imposed density floor is lowered from $10^{-4}\rho_0$ to $10^{-5}\rho_0$; when the box size is doubled horizontally; or when the box height varies from $12H$ to $10H$ or $14H$ (Table 1). Increasing the spatial resolution tends to increase the Reynolds stress and lower the gravitational stress. Velocity fluctuations are better resolved with finer grids, but the gains are modest; doubling the resolution in all directions changes non-circular velocities by ∼30% at most and typically by only several percent; at the same time, the increased Reynolds stress should be offset by a decrease in gravitational stress, since the total heating rate must balance the imposed cooling rate (see Figure 4). Note that simulations with larger β (longer cooling times) have smaller amplitude fluctuations and are more computationally demanding—this may be the reason why, e.g., our $\beta = 80$ runs exhibit more sensitivity to resolution than our $\beta < 80$

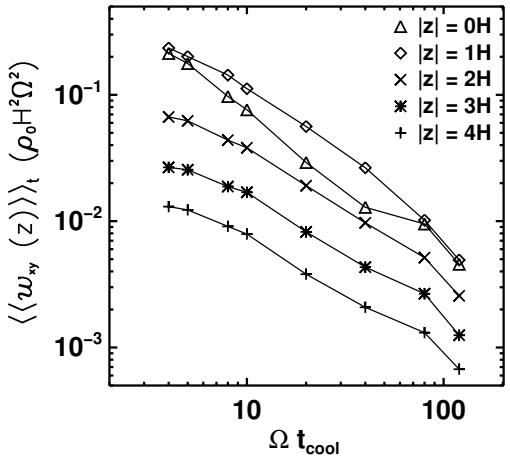

Fig. 5.— Time-averaged total absolute stress (not normalized by pressure) as a function of cooling time for our high-resolution constant β runs, for various disk heights. In making this plot, we average data above and below the midplane, and over a time interval lasting $> 2t_{\rm cool}$ at the end of each simulation (see Table 1). Stresses tend to decrease with height, but only by factors of ∼6–16 from $z = 0$ to $|z| = 4H$, while the density drops by nearly 10^3. In Figure 6 we will see that the gravitational stress at altitude is exerted largely by density fluctuations at the midplane. The time-averaged stress actually peaks slightly away from the midplane because the Reynolds stress at the midplane alternates in sign periodically, leading to a partial cancellation in the time average there.

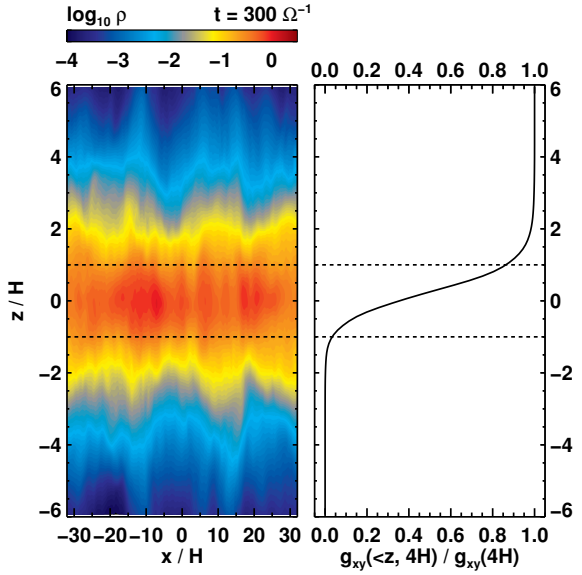

Fig. 6.— Contributions from all heights to the gravitational stress $g_{xy} \equiv g_x g_y / 4\pi G$ at $z = +4H$. *Left*: Poloidal snapshot of the azimuthally averaged log density at $t = 300\Omega^{-1}$ from our $\beta = 10$ high resolution run. *Right*: the running fraction of the gravitational stress at $+4H$ from heights less than z; by definition, this fraction is zero for $z = -6H$ (there is no disk material below the bottom of our box) and unity for $z = 6H$ (all material is contained below the top of our box). Dashed lines show where $z = \pm H$. The lion's share of the stress at $+4H$ originates from between $z = -H$ and $z = +H$, where more than 75% of the disk mass resides.

runs (see Table 1). Unless indicated otherwise, the data plotted in all our figures and discussed in the text are drawn from our high resolution simulations with a standard density floor of $10^{-4}\rho_0$ (i.e., the .hi models in Table 1).

3.1.3. Turbulent Velocities vs. Height

The variation with height of the rms value of the turbulent velocity δv (i.e., the non-Keplerian bulk motion) is shown in Figure 7 for $\beta = 10$. Turbulent velocities vary only weakly with altitude, increasing by less than a factor of two from midplane to surface as the overlying column density drops by more than three orders of magnitude. That turbulent motions are just as vigorous at altitude as they are at depth might at first glance seem surprising, since densities at altitude fall below the Toomre density $\Omega^2/2\pi G \sim 0.5$ (Shi & Chiang 2013). In other words, gas at altitude is not self-gravitating and does not generate turbulence in and of itself. But in hindsight, the relatively flat velocity profile is understandable, because as we noted in section 3.1.2, gravity is long-range: density fluctuations at the midplane—where gas is of Toomre density and is self-gravitating—exert gravitational forces at altitude and strongly perturb the rarefied gas there.

In fact, non-Keplerian motions are, if anything, greater at altitude than at depth. Vertical velocities v_z vary more strongly with height (factor of 5 increase from midplane to surface) than do in-plane velocities $v_{\rm p}$, [2] which is sensible because the

[2] As shown in Figure 7, the drop in the vertical component of turbulent velocity from $|z| \approx 5H$ to $6H$ in our standard box is a numerical artifact, as we have discovered by vary-

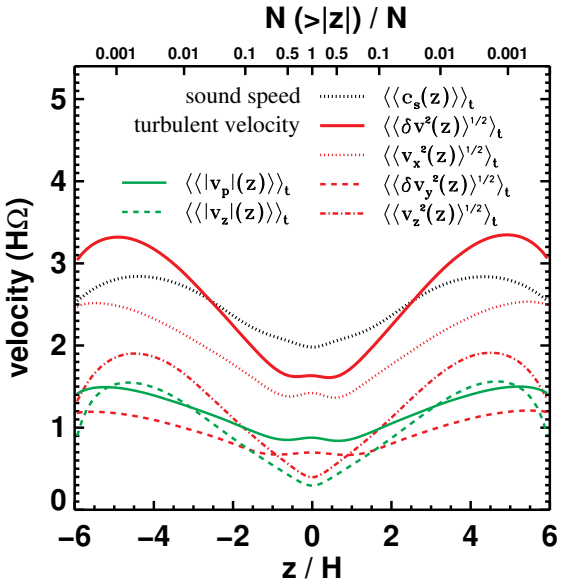

Fig. 7.— Vertical profiles of the sound speed and turbulent (read: non-circular) velocities, time-averaged from $t = 200$–$300\Omega^{-1}$ using our high-resolution $\Omega t_{\rm cool} = 10$ run (tc=10.hi). Neither the sound speed nor the turbulent velocities vary much with height, even as the overlying column density above a given height (measured on the top x-axis) drops by three orders of magnitude. Red curves denote individual components of rms turbulent velocities, while green curves denote our proxies for line-of-sight turbulent velocities, as defined in §3.1.3. Here and elsewhere, we discount the behavior at $|z| \gtrsim 5H$ as it is sensitive to our vertical box boundary conditions. By contrast, results at $-5H < z < 5H$ are far enough away from the vertical boundaries to be robust; see Figure 8.

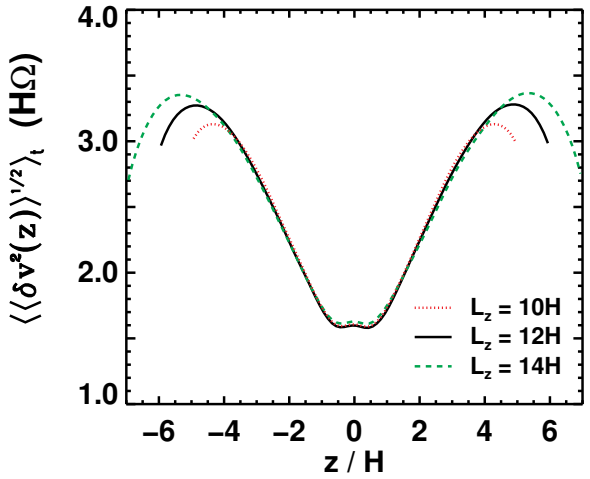

Fig. 8.— Vertical profiles of rms turbulent velocity $\langle\langle \delta v^2(z)\rangle^{1/2}\rangle_t$ for simulations with different box heights L_z. The fact that in all simulations, velocities roll over $\sim 1H$ away from box boundaries indicates that the velocity behavior there is spurious and subject to artificial boundary effects. Consequently, throughout this paper, when we discuss our results for our standard box having $L_z = 12H$, we restrict our statements to $|z| \lesssim 5H$.

vertical gravitational acceleration from disk self-gravity tends to increase away from the midplane: at the midplane, vertical forces from the upper and lower disk tend to cancel. In addition, fluid motions in all directions should amplify at altitude from the steepening of waves launched upward from the midplane and which propagate down density gradients. Simon et al. (2011) suggested from their numerical experiments that increasing velocity dispersions with height are generic to turbulent disks, and our results are consistent with this proposal. At $|z| > H$, motions are strongest in the x-z plane, driven by self-gravity in those directions; azimuthal perturbations are suppressed by Keplerian differential rotation which shears overdensities into nearly axisymmetric structures. We see evidence for a kind of x-z circulation, whereby gas compresses radially from self-gravity and spurts out vertically, as illustrated in Figure 9.

We also calculate velocity dispersions more closely related to observables. We forego a full spectral line analysis and instead compute a line-of-sight (los) turbulent velocity in the disk plane, averaged over azimuth ϕ:

$$|v_{\rm p}| \equiv \frac{1}{2\pi}\int_0^{2\pi} d\phi\, |v_{\rm x}\cos\phi - \delta v_{\rm y}\sin\phi| \qquad (22)$$

(Simon et al. 2011; Forgan et al. 2012). Here we use $\delta v_{\rm y}$ for the turbulent velocity in the azimuthal direction, not to be confused with the bulk velocity $v_{\rm y}$ which includes the background shear ve-

ing the box height to $10H$ (run tc=10.hi.lz10) and $14H$ (tc=10.hi.lz14)—see Figure 8. For any given box, the total rms turbulent velocity rolls over at a distance of $\sim 1H$ from either vertical boundary. The roll-over might be due to the enforced outflow boundary conditions that artificially eliminate any inward motion. Conversely, our results away from the vertical boundaries appear to have converged with box size.

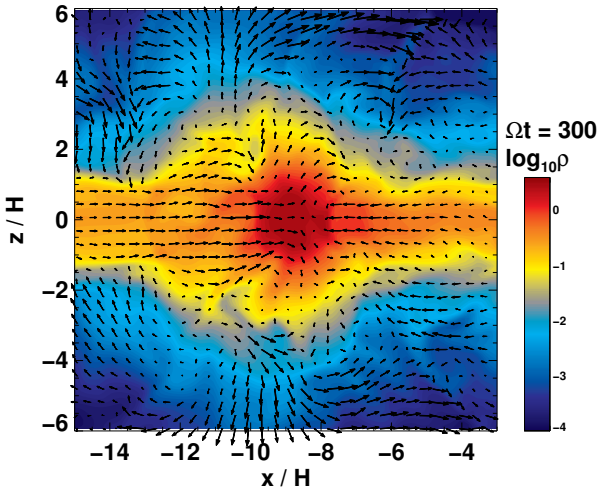

Fig. 9.— A meridional snapshot, taken at $t = 300\Omega^{-1}$ and fixed azimuth $y = 0$, of our high-resolution $\Omega t_{\rm cool} = 10$ run (tc=10.hi). Colors show log density and arrows show the velocity field. The longest arrow has an x-z velocity of $8.17H\Omega$, or 1.45 of the local sound speed. These velocities are within a few percent of the total 3D non-circular velocities, as contributions from δv_y are typically small.

locity. The quantity $|v_{\rm p}|$ is a proxy for the actual los turbulent linewidth for disks seen edge-on. For disks seen face-on, the corresponding proxy velocity is $|v_z|$. Figure 7 plots the vertical profiles for $\langle|v_{\rm p}(z)|\rangle$ and $\langle|v_z(z)|\rangle$ (each horizontally averaged), while the top left panel of Figure 10 displays the full probability density functions for $|v_{\rm p}|/c_{\rm s}$ and $|v_z|/c_{\rm s}$ for several cuts in height, all for $\beta = 10$. There is little variation in these proxy los velocities with height, particularly for $|v_{\rm p}|$. The most probable value of $|v_{\rm p}|/c_{\rm s}$ increases by a factor of only 1.2 from $z > 0$ to $z > 4H$ (for $\beta = 10$), while $|v_z|/c_{\rm s}$ increases by a factor of 2.5. We obtain similarly flat velocity profiles for all $\beta > 3$ runs; the only difference is a systematic shift toward smaller velocities as $t_{\rm cool}$ increases, e.g., for $\beta = 10(40)$, the most probable value of $|v_{\rm p}|/c_{\rm s}$ is 0.35(0.22), sampled over all $z > 0$; see Figure 10).[3]

[3]Forgan et al. (2012) also reported in their global simulations of self-gravitating disks that turbulent velocity distributions are virtually unchanged from $z > 0$ to $z > H$; see their Figure 3, and note that their turbulent velocities and stresses are considerably lower than ours, presumably because the cooling times of their disks are much longer. They observed that the linewidth probability distributions sampled at different heights were "remarkably similar, but the poor resolution of higher altitudes forbids us from attributing this to any phenomenology of the disc." By comparison, our local simulations are well resolved vertically and show that the flatness of the turbulent velocity profile extends more than three orders of magnitude in column density from midplane to disk surface.

Note that the variations in Mach numbers between simulations with different cooling times are almost all due to variations in turbulent velocities, not to variations in the sound speed. Table 1 indicates that the sound speeds of various simulations are all about the same—as expected, since the input surface densities and self-regulated Toomre Q-values are all about the same, irrespective of cooling time. Prolonging the cooling time reduces turbulent velocities but does not alter background temperatures (at fixed surface density).

Figure 10 also makes a head-to-head comparison between the velocity distributions of our gravito-turbulent disks and those of a disk made turbulent by the magneto-rotational instability (MRI). Our MRI data are extracted from the standard run (STD32) of Shi et al. (2010), who studied the MRI using a stratified, non-self-gravitating, ideal MHD shearing box with zero net magnetic flux (for details, see their sections 2 and 3.1). Turbulent velocities vary more strongly with height in MRI-turbulent disks than in gravito-turbulent disks; as z increases from the midplane and the overlying column density drops by three orders of magnitude, both $|v_{\rm p}|/c_{\rm s}$ and $|v_z|/c_{\rm s}$ increase in the MRI-turbulent disk by factors of $\sim$15, from $\sim$0.06 to $\sim$1. This variation characterizes ideal MHD disks. Similar results, including supersonic velocities at $z > 3H$, were obtained by Simon et al. (2011). In non-ideal disks (those affected by Ohmic dissipation, ambipolar diffusion, and/or the Hall effect), the variation of magnetically driven velocities with altitude tends to be even steeper (Simon et al. 2011, 2013a; see also Figure 7 of Lesur et al. 2014).

Forgan et al. (2012) suggested that the ratio $|v_{\rm p}|/|v_{\rm z}|$ could be used to differentiate between gravito-turbulent and MRI-turbulent disks. They found that $|v_{\rm p}| \sim 6|v_{\rm z}|$ near the midplanes of their gravito-turbulent disks, whereas MHD turbulence is more isotropic (even at the midplane of a dead zone, $|v_{\rm p}|$ differs from $|v_{\rm z}|$ by a factor $\lesssim 3$ accord-

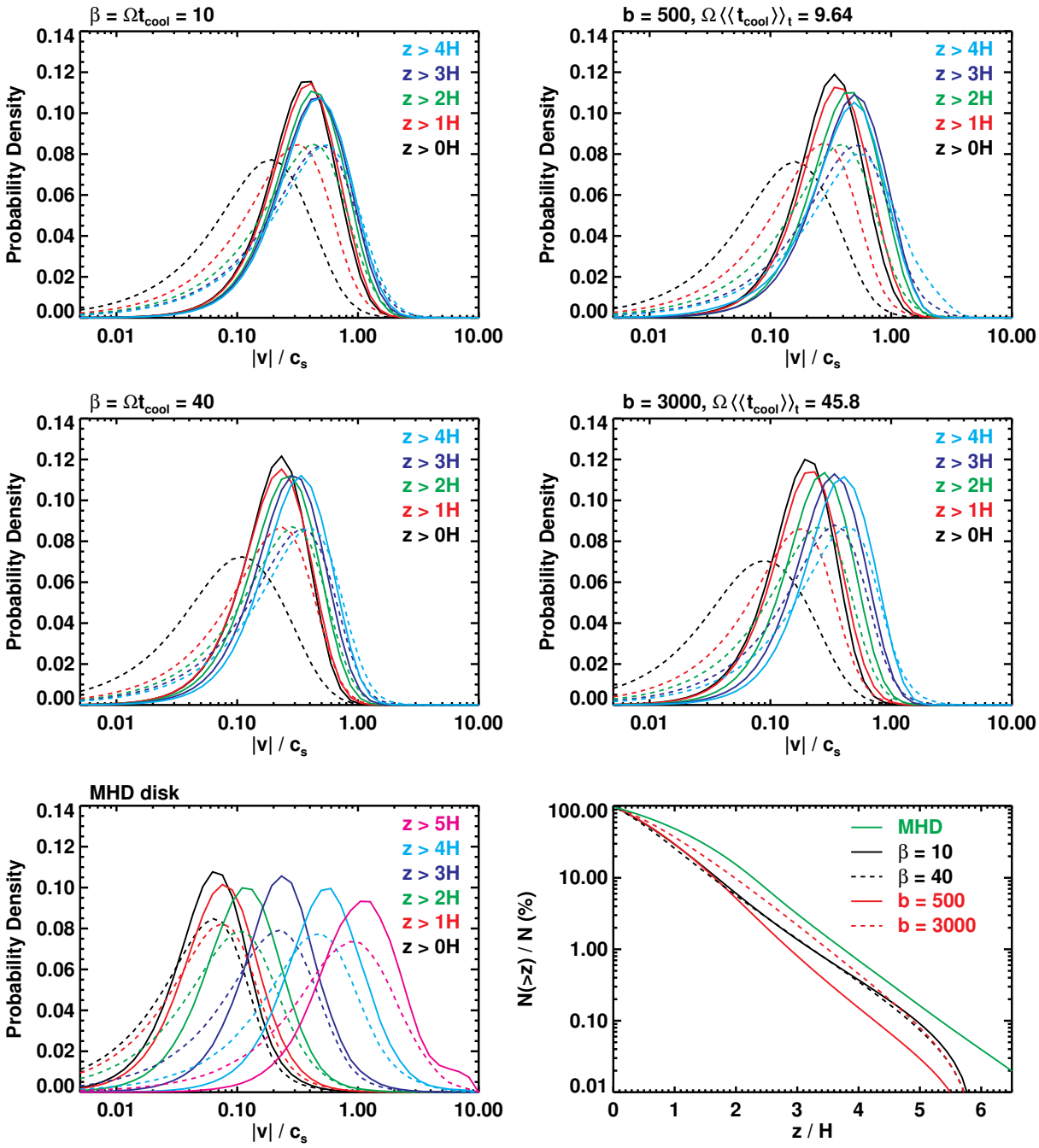

Fig. 10.— Probability density distributions, sampled at various heights, of in-plane turbulent Mach numbers ($|v_{\rm p}|/c_{\rm s}$, solid curves) and vertical turbulent Mach numbers ($|v_{\rm z}|/c_{\rm s}$, dashed curves), for constant $\beta \in \{10, 40\}$ and optically-thin $b \in \{500, 3000\}$ simulations, as labeled. Probability densities are probabilities per unit log Mach number. Also shown for comparison are results from an MRI-turbulent disk, run STD32 of Shi et al. (2010). How the fractional overlying column density $N(> z)/N$ varies with height z for each model is shown at bottom right. Gravito-turbulent velocities vary less with height than do MHD-turbulent velocities.

ing to the top panel of Figure 4 of Simon et al. 2011). Our results are nominally of higher resolution, and show that $|v_{\rm p}|$ is indeed higher than $|v_{\rm z}|$, but only by factors of 2–3 at the midplane (Figure 10). Unfortunately, even this difference appears to vanish at altitude. Thus the usefulness of $|v_{\rm p}|/|v_{\rm z}|$ in distinguishing between gravito-turbulence and MRI turbulence appears limited.

3.2. Optically-Thin Thermal Cooling

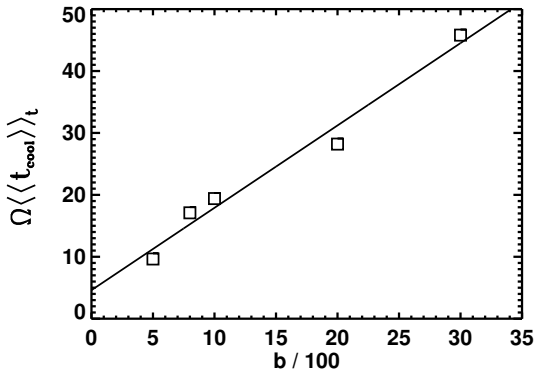

Fig. 11.— Relation between the b-parameter (equation 8) of our optically-thin thermal cooling experiments, and the effective cooling time (equation 23). Squares represent simulation results, while the solid line is the best linear fit ($\Omega\langle\langle t_{\rm cool}\rangle\rangle_t = 0.0113b + 4.61$, with b in code units). The linear relation reflects the fact that our adopted cooling rate scales strongly with T (as T^4) and tends to thermostat disks to the same temperature, regardless of b and regardless of height.

Initial conditions for each of our optically-thin cooling experiments (section 2.1) are taken from our constant cooling time simulation tc=10.hi at $t = 160\Omega^{-1}$. Optically-thin cooling is turned on immediately, with the cooling parameter $b \in \{100, 500, 800, 1000, 2000, 3000\}$ in code units; see equation (8). For every b, we can compute an effective cooling time

$$\langle\langle t_{\rm cool}\rangle\rangle_t \equiv \frac{\langle\langle U\rangle\rangle_t}{\langle\langle \rho\mathcal{L}\rangle\rangle_t}\,. \qquad (23)$$

Figure 11 shows that b scales linearly with $\langle\langle t_{\rm cool}\rangle\rangle_t$. Our optically thin disks quickly settle into new gravito-turbulent states, except in the $b = 100$ run, where the disk cools so rapidly ($\langle\langle t_{\rm cool}\rangle\rangle_t \lesssim 3\Omega^{-1}$) that it fragments. For $b > 100$, we recover the nearly inverse-linear scaling between stress and cooling time (see Table 1). When computing averages, we sample data after the disk settles into steady gravito-turbulence, and use time intervals lasting $\sim$100–150 Ω^{-1} or $\gtrsim 3$–$10\langle\langle t_{\rm cool}\rangle\rangle_t$.

In general, our optically-thin thermally cooling disks behave similarly to our constant $t_{\rm cool}$ disks. For example, $\langle\alpha\rangle_t = 0.0566$ for $b = 500$ ($\langle\langle t_{\rm cool}\rangle\rangle_t = 9.6\Omega^{-1}$), and $\langle\alpha\rangle_t = 0.0552$ for $\beta = 10$ ($t_{\rm cool} = 10\Omega^{-1}$). For both prescriptions, cooling is local; furthermore, since our optically thin disks have cooling times that depend only on temperature — i.e., $t_{\rm cool} \propto b/T^3$ — their cooling times are effectively constant as long as the disks are nearly isothermal. In fact, Figure 12 shows that our optically thin disks are more uniform in temperature than our constant cooling time disks at $|z| < 4H$, presumably because the cooling flux increases rapidly as T^4 and thermostats the gas.

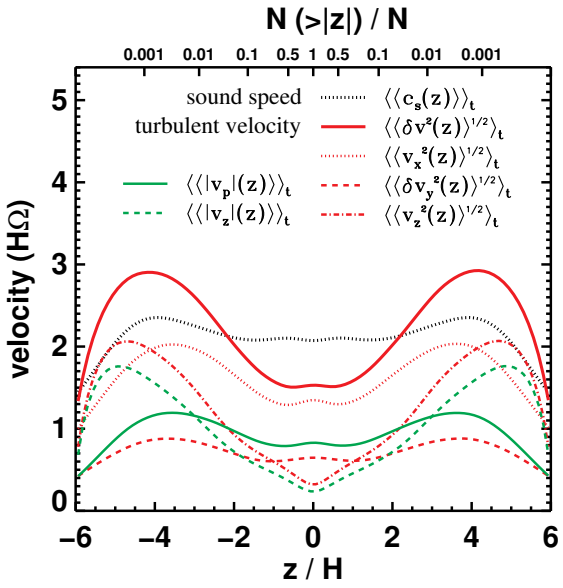

Fig. 12.— Turbulent velocity and sound speed profiles for our simulation using optically-thin thermal cooling with $b = 500$ (run b=500.hi). As was the case in our constant cooling time experiments (Figure 7), turbulent velocities and sound speeds change only modestly with height. Here and elsewhere, we ignore our results at $|z| > 5H$ because of numerical boundary effects; by contrast, the behavior at $-5H < z < 5H$ is robust to changes in box size.

As was the case for our constant β disks, turbulent velocities of optically thin disks vary modestly with height. For example, in-plane velocities increase by a factor of 1.5 from $|z| = 0$ to $4H$, and vertical velocities increase by a factor of 5, even while the density drops by three orders of magnitude. Probability distributions for the in-plane and vertical Mach numbers are displayed in Figure 10. These distributions shift toward smaller Mach numbers as b increases (i.e., as the opacity decreases and the cooling time increases): the most probable value of $|v_{\rm p}|/c_{\rm s}$ (sampled over all $|z| > 0$) changes from 0.31 for $b = 500$ to 0.2 for $b = 3000$.

4. SUMMARY AND DISCUSSION

We used local shearing box simulations to study optically thin, cooling, gravito-turbulent disks. Our investigation is basically the 3D version of Gammie's (2001) study. Our main result is that non-circular motions driven by gravito-turbulence are nearly independent of height above the midplane, across density contrasts as large as 10^3. The insensitivity of turbulent velocity to height is due to gravity's long-range nature. Although gas at altitude is too rarefied to be itself self-gravitating, it is strongly gravitationally accelerated by Toomre-density fluctuations near the midplane. This behavior contrasts with that in disks made turbulent by the magneto-rotational instability (MRI). In MRI-unstable disks, non-circular velocities increase by more than a factor of 10 from midplane to surface, and velocity variations are even larger when non-ideal magnetohydrodynamic effects are present. Our theoretical results, coupled with empirical measurements of non-thermal line broadening in protoplanetary disks, promise to distinguish between gravito-turbulence and MRI turbulence—or perhaps to rule out both in favor of some other transport mechanism (Hughes et al. 2011; Hughes et al. 2014, in preparation).

Our results were derived under the assumption that the disk is optically thin to its own cooling radiation. We obtained similar simulation outcomes by assuming either a fixed cooling time or a cooling time that depends on the local temperature. To avoid fragmentation, these cooling times must exceed the local dynamical time. Optically thin, self-gravitating disks with cooling times longer than their dynamical times may not be too hard to find in nature, at least among protoplanetary disks.[4] At an orbital distance of $R \sim 100$ AU from a solar-mass star, a surface density of $\Sigma \sim 10$ g/cm^2 (i.e., a disk mass of $\Sigma R^2 \sim 0.01 M_\odot$) and a temperature of $T \sim 10$ K leads to a Toomre Q on the order of unity. The optical depth and cooling time depend on the dust opacity κ, which is notoriously uncertain, as it depends on the grain size distribution and the dust-to-gas ratio. At the sub-millimeter wavelengths characterizing most of the cooling radiation from the outer disk, values for κ range from 10^{-3} to 10^{-1} cm^2/g (D'Alessio et al. 2001, their Figure 1), depending on how large grains have grown; actual values would be lower if dust were depleted relative to gas as a result of radial drift (e.g., Andrews et al. 2012). If we adopt $\kappa \sim 10^{-2}$ cm^2/g, then the optical depth of our example disk would be $\tau = \Sigma\kappa \sim 0.1$ and the cooling time would be $10^3(\Sigma/10\,{\rm g\,cm^{-2}})(10\,{\rm K}/T)^3(0.1/\tau)$ yr, about six times longer than the local dynamical time $\Omega^{-1} \sim 160$ yr. Such a disk falls squarely within the domain explored by our optically-thin cooling simulations: for $R = 100$ AU and $T = 10$ K, our $b = 500$ run corresponds to an effective cooling time of $9.64\Omega^{-1}$ and $\kappa \sim 6 \times 10^{-3}$ cm^2/g.

Recently the long-term stability of gravito-turbulent disks has been questioned (Paardekooper 2012; Hopkins & Christiansen 2013). The standard criteria for fragmentation are $\Omega t_{\rm cool} \lesssim 3$ and $Q \lesssim 1$ (e.g., Gammie 2001), but a more complete assessment of stability should account for statistical fluctuations which can generate Toomre-unstable overdensities over long enough time intervals (Hopkins & Christiansen 2013). We did not focus in this paper on the dynamics of collapse. In nearly all of the parameter space that we explored ($\Omega t_{\rm cool} \geq 4$, $\gamma = 5/3$, $t \sim 100$–$500\Omega^{-1}$), our 3D simulations did not show collapse. There were only two simulations which resulted in fragmentation: constant cooling with $\beta = 3$ and optically-thin cooling with $b = 100$ (effective cooling times $\lesssim 3\Omega^{-1}$). Our results confirm that the standard collapse criterion $\Omega t_{\rm cool} \lesssim 3$ applies over timescales up to dozens of orbits.

[4] Disks in active galactic nuclei become gravitationally unstable at such large radii and where surface densities are so low that their local cooling times are too short to maintain quasi-steady gravito-turbulence (Goodman 2003; but see Bertin & Lodato 2001 for an alternative view).

Some next steps for this work include treating optically thick disks; accounting for stellar irradiation; and resolving radial structure, perhaps with global simulations that can track non-local energy and angular momentum transport. Studies like those by Forgan et al. (2012), Kratter & Murray-Clay (2011), Meru & Bate (2010), Forgan & Rice (2010), Rafikov (2009), Lodato & Rice (2005), and Lodato & Rice (2004) push on these fronts, but lack the vertical resolution that our local, optically thin simulations enjoy. We suspect, however, that the inclusion of additional physics will not change our finding that gravito-turbulent velocities change by less than a factor of 2 with vertical height. Optically thick disks will have stronger vertical variations in cooling time than optically thin disks, but the only cooling time that matters for determining the overall vigor of gravito-turbulence should be that averaged over the first scale height of the disk; only here is material actually dense enough to be gravitationally unstable. Whether the disk is optically thick or thin has no bearing on the fact that material at a given radius and height can be strongly perturbed by density fluctuations at the midplane, either at the same radius or elsewhere. It is the long-range connectivity enabled by self-gravity that renders turbulent motions the same at altitude as at depth.

We thank Meredith Hughes for motivating discussions, and Yan-Fei Jiang and Chang-Goo Kim for confirming the boundary problem with `Athena`'s shearing-box Poisson solver. Phil Armitage, Xue-Ning Bai, Duncan Forgan, Charles Gammie, Yan-Fei Jiang, Sijme-Jan Paardekooper, Jake Simon, and Jim Stone provided helpful and encouraging comments on a draft manuscript. We also thank an anonymous referee for a careful and thorough report. Financial support was provided by a NASA Origins grant. Resources supporting this work were provided by the NASA High-End Computing (HEC) Program through the NASA Advanced Supercomputing (NAS) Division at Ames Research Center.

REFERENCES

Andrews, S. M., Wilner, D. J., Hughes, A. M., Qi, C., Rosenfeld, K. A., Öberg, K. I., Birnstiel, T., Espaillat, C., Cieza, L. A., Williams, J. P., Lin, S.-Y., & Ho, P. T. P. 2012, ApJ, 744, 162

Bai, X.-N. 2011, ApJ, 739, 50

—. 2013, ApJ, 772, 96

Bai, X.-N. & Stone, J. M. 2013, ApJ, 769, 76

Balbus, S. A. & Hawley, J. F. 1991, ApJ, 376, 214

—. 1998, Reviews of Modern Physics, 70, 1

Bell, K. R. & Lin, D. N. C. 1994, ApJ, 427, 987

Bertin, G. & Lodato, G. 2001, A&A, 370, 342

Clarke, C. J., Harper-Clark, E., & Lodato, G. 2007, MNRAS, 381, 1543

Cossins, P., Lodato, G., & Clarke, C. J. 2009, MNRAS, 393, 1157

D'Alessio, P., Calvet, N., & Hartmann, L. 2001, ApJ, 553, 321

Forgan, D., Armitage, P. J., & Simon, J. B. 2012, MNRAS, 426, 2419

Forgan, D. & Rice, K. 2010, MNRAS, 402, 1349

Gammie, C. F. 2001, ApJ, 553, 174

Goodman, J. 2003, MNRAS, 339, 937

Hartmann, L., D'Alessio, P., Calvet, N., & Muzerolle, J. 2006, ApJ, 648, 484

Hopkins, P. F. & Christiansen, J. L. 2013, ApJ, 776, 48

Hughes, A. M., Wilner, D. J., Andrews, S. M., Qi, C., & Hogerheijde, M. R. 2011, ApJ, 727, 85

Jiang, Y.-F., Belyaev, M., Goodman, J., & Stone, J. M. 2013, New A, 19, 48

Johnson, B. M. & Gammie, C. F. 2003, ApJ, 597, 131

Johnson, B. M., Guan, X., & Gammie, C. F. 2008, ApJS, 177, 373

Kim, C.-G., Kim, W.-T., & Ostriker, E. C. 2011, ApJ, 743, 25

Koyama, H. & Ostriker, E. C. 2009, ApJ, 693, 1316

Kratter, K. M. & Murray-Clay, R. A. 2011, ApJ, 740, 1

Kunz, M. W. & Lesur, G. 2013, MNRAS, 434, 2295

Laughlin, G., Steinacker, A., & Adams, F. C. 2004, ApJ, 608, 489

Lee, A. T., Chiang, E., Asay-Davis, X., & Barranco, J. 2010a, ApJ, 718, 1367

—. 2010b, ApJ, 725, 1938

Lesur, G., Kunz, M. W., & Fromang, S. 2014, ArXiv e-prints

Lodato, G. & Rice, W. K. M. 2004, MNRAS, 351, 630

—. 2005, MNRAS, 358, 1489

Masset, F. 2000, A&AS, 141, 165

Mejía, A. C., Durisen, R. H., Pickett, M. K., & Cai, K. 2005, ApJ, 619, 1098

Meru, F. & Bate, M. R. 2010, MNRAS, 406, 2279

—. 2011, MNRAS, 411, L1

—. 2012, MNRAS, 427, 2022

Nelson, R. P. & Papaloizou, J. C. B. 2004, MNRAS, 350, 849

Ormel, C. W., Spaans, M., & Tielens, A. G. G. M. 2007, A&A, 461, 215

Paardekooper, S.-J. 2012, MNRAS, 421, 3286

Paczynski, B. 1978, Acta Astron., 28, 91

Perez-Becker, D. & Chiang, E. 2011a, ApJ, 735, 8

—. 2011b, ApJ, 727, 2

Rafikov, R. R. 2009, ApJ, 704, 281

Rein, H. 2012, MNRAS, 427, L21

Rice, W. K. M., Armitage, P. J., Bate, M. R., & Bonnell, I. A. 2003, MNRAS, 339, 1025

Rice, W. K. M., Paardekooper, S.-J., Forgan, D. H., & Armitage, P. J. 2014, MNRAS

Shi, J., Krolik, J. H., & Hirose, S. 2010, ApJ, 708, 1716

Shi, J.-M. & Chiang, E. 2013, ApJ, 764, 20

Simon, J. B., Armitage, P. J., & Beckwith, K. 2011, ApJ, 743, 17

Simon, J. B., Bai, X.-N., Armitage, P. J., Stone, J. M., & Beckwith, K. 2013a, ApJ, 775, 73

Simon, J. B., Bai, X.-N., Stone, J. M., Armitage, P. J., & Beckwith, K. 2013b, ApJ, 764, 66

Stone, J. M. & Gardiner, T. 2009, New A, 14, 139

Stone, J. M. & Gardiner, T. A. 2010, ApJS, 189, 142

van Leer, B. 2006, Comm. Comput. Phys., 1, 192

Wardle, M. & Salmeron, R. 2012, MNRAS, 422, 2737

This 2-column preprint was prepared with the AAS LaTeX macros v5.2.